Advanced Materials

ADVANCED MATERIALS
www.advmat.de

RESEARCH ARTICLE

Ultrasonic Vibration-Driven Cold Upcycling of Waste Plastics: Enabling High-Efficiency Seawater Distillation

Shengyu Zhao[1,2,3] | Shike Huang[1] | Shuzhe Zhang[4] | Junsheng Liu[1] | Jianan Fu[5] | Boyang Wu[1] | Wenzhe Bao[1] | Xiangyang Yu[1] | Jiasen Sun[1] | Kangyu Lin[1] | Jinbiao Huang[1] | Bangliang Cao[1] | Xingran Zhao[1] | Wenqing Ruan[1] | Xiaodi Liu[1] | Chaoqun Pei[1] | Jiang Ma[1,2,3]

[1]State Key Laboratory of Radio Frequency Heterogeneous Integration, Shenzhen University, Shenzhen, China | [2]Shenzhen Key Laboratory of High Performance Nontraditional Manufacturing, Shenzhen University, Shenzhen, China | [3]Guangdong Provincial Key Laboratory of Micro/Nano Optomechatronics Engineering, Shenzhen University, Shenzhen, China | [4]Department of Chemical Engineering and Applied Chemistry, College of Chemistry, Jilin University, Changchun, China | [5]Department of Mechanics and Aerospace Engineering, Southern University of Science and Technology, Shenzhen, Guangdong, China

Correspondence: Jiang Ma (majiang@szu.edu.cn)

Received: 5 December 2025 | **Revised:** 29 April 2026 | **Accepted:** 18 May 2026

Keywords: cold fabrication | plastic upcycling | porous carbon | seawater distillation | ultrasonic vibration

ABSTRACT

Plastic pollution has become a pervasive environmental crisis, intensifying greenhouse gas emissions, contaminating soils, and potentially aggravating cardiovascular risks. Prevailing recycling strategies such as incineration, landfilling, and mechanical processing remain constrained by inefficiency, contamination, and excessive energy demand, resulting in limited reusability of the recovered materials. Therefore, developing an eco-friendly, high-performance technology that transforms plastic waste into valuable resources is imperative. Herein, we report a novel waste plastic upcycling strategy utilizing ultrasonic vibration cold fabrication to convert waste polyethylene terephthalate into carbon materials. The polyethylene terephthalate was treated via a combination of ultrasonic vibration and dissolution methods to produce highly carbonized, porous materials with high photothermal efficiency that enable high-performance seawater distillation. High-frequency stress treatment promotes rapid polymer chain scission, deoxygenation, and aromatization, facilitating heat-source-free carbonization. We further revealed that porous carbonized materials exhibit exceptional broadband photothermal conversion with an efficiency exceeding 95%. In seawater distillation, the material generated 2.19 kg m^{-2} h^{-1} of solar steam and maintained stability in high-salinity conditions. Leveraging the flexible fabrication capability of these porous carbons, we constructed a solar evaporation device and demonstrated a freshwater yield of 6.02 kg m^{-2} in 10 h of outdoor testing, which is 5.2 times that of natural evaporation.

1 | Introduction

Plastics are essential in modern life due to their low cost, light weight, and durability, playing a key role across various sectors such as electronics, packaging, construction, and healthcare [1, 2]. 500 Mt yr^{-1} of global plastic production has already been surpassed, and it is expected to triple by 2050 if left unchecked [3–5]. However, the current management of plastic waste has not kept pace with production, leading to widespread mismanagement of post-consumer plastics. These plastics accumulate in landfills, rivers, and oceans, fragmenting into persistent microplastics that pose severe ecological and human health risks [3, 4, 6–9]. These trends elevate plastics from a conventional solid-waste issue to a major environment-and-climate challenge, underscoring the urgent need to move away from disposal and toward efficient recycling and high-value upcycling [10, 11]. Traditional recycling strategies, including mechanical reprocessing, energy recovery, and chemical recycling, each come with significant drawbacks.

Mechanical recycling, while the most widely used, leads to material degradation after multiple cycles, limiting its suitability for high-value applications [12–15]. Energy recovery through incineration reduces waste volume but releases large amounts of greenhouse gases like CO_2, exacerbating the greenhouse effect [16, 17]. Chemical recycling methods, such as pyrolysis, gasification, and solvolysis, can break plastics down into smaller molecules, but their practical implementation remains hindered by high energy demands, harsh reaction conditions, and low-value outputs [18–21]. These methods also rely on catalysts that are costly, difficult to synthesize, and prone to deactivation, creating additional barriers to their sustainable deployment [22, 23]. In parallel, biological upcycling offers mild operating conditions and potentially high product selectivity, yet remains constrained by intrinsically slow kinetics and the stability/efficiency of enzymes and microbial systems, which currently limit throughput and scale-up for real-world plastic streams [24]. As a result, there is an urgent need for a cost-effective, efficient, and environmentally friendly solution to address the growing plastic pollution crisis.

Against this backdrop, the conversion of plastic waste into carbon materials has recently emerged as a promising upcycling route. Plastics, being inherently carbon-rich polymers, lend themselves well to carbonization, a process that transforms them into solid carbon frameworks, preventing the release of CO_2 into the atmosphere and offering the potential for long-term carbon storage [25–28]. Carbonization also generates porous carbons with tunable microstructures and functional properties, opening up a wide range of applications in adsorption, catalysis, energy storage, and photothermal water evaporation [29–31]. Notably, such porous carbons serve as a commercially established benchmark material, typically priced at approximately USD 1.8–2.47 kg^{-1} and supported by a mature global market valued at around USD 4.46 billion in recent years, thus highlighting the strong economic viability of plastic-to-carbon upcycling. For example, porous carbons with hierarchical micro–meso–macro porosity can provide abundant active sites and fast transport channels, making them ideal for use as electrodes, adsorbents, or photothermal layers [28, 32–34]. Despite these advantages, current carbonization methods still face huge challenges. Traditional techniques such as pyrolysis and activation operate at high temperatures (800–1300 K) for several hours, requiring a nitrogen or argon atmosphere, which makes them energy-intensive and costly [35]. Chemical activation with agents like KOH or NaOH increases the material's porosity but involves corrosive reagents and complex wastewater management [36]. Catalytic graphitization lowers the temperature but introduces metal recovery steps, while hard/soft templating requires etching. Although hydrothermal routes are milder (450–570 K), they yield oxygen-rich hydrochars that often require further high-temperature treatment or activation to enhance their properties [37]. More recently, flash Joule heating has enabled rapid processing within seconds. However, its reliance on high-peak-power electrical pulses and specialized hardware imposes significant challenges for scalability and energy distribution [38]. These limitations underscore the need for a new approach—one that facilitates low-energy, high-efficiency carbonization with minimal external heat, capable of directly producing high-quality, device-grade porous carbons from plastic waste. Ultrasonic vibration (USV) represents a unique material processing technique, which enables the rapid preparation and fabrication of materials through high-frequency mechanical vibration [39, 40]. Benefiting from its low heat generation during treatment and the mature industrial feasibility for mass production, USV exhibits promising application prospects in the rapid recycling of waste plastics.

In this work, we present this novel upcycling strategy for waste plastics, utilizing USV cold fabrication to convert polyethylene terephthalate (PET) waste into carbon materials with exceptional photothermal efficiency. This approach enables high-performance seawater distillation, offering a sustainable solution to plastic waste and water scarcity. Through the combination of USV with a dissolution method, we successfully prepared highly carbonized and porous materials from PET (USV-PET), achieving a rapid (<60 s) conversion into porous carbon without the need for external heat sources. The dissolution method further creates interconnected hierarchical pores, enhancing USV-PET structure for optimized performance. The synergistic interaction between Zinc oxide (ZnO) and high-frequency stress during USV treatment accelerates polymer chain scission, deoxygenation, and aromatization, which facilitates heat-source-free carbonization. Our findings show that USV-PET exhibits outstanding broadband photothermal conversion efficiency exceeding 95%, making it ideal for solar-driven applications. Moreover, USV-PET demonstrates excellent seawater distillation and salt resistance, generating 2.49 kg m^{-2} h^{-1} of solar steam while maintaining stability under high-salinity conditions. Notably, the ion concentration of the desalinated water is significantly lower than the international drinking water standards. Leveraging the flexibility of USV-PET, we construct a solar evaporation device that achieves a remarkable fresh water yield of 6.02 kg m^{-2} in just 10 h of outdoor testing, 5.2 times higher than natural evaporation. This study introduces USV cold fabrication as a transformative method for the high-value upcycling of waste plastics, offering a promising solution for both sustainable energy production and environmental protection.

2 | Results and Discussion

2.1 | Fabrication and Characterization of USV-PET

Figure 1a schematizes the fabrication process of USV-PET. A homogeneous PET/ZnO powder mixture was loaded into a stainless-steel die and subjected to USV under a frequency of 20 kHz, during which the initially white mixture rapidly turned into black, brittle carbon particulates. The particulates were ground and hot-pressed to obtain a dense bulk intermediate. Subsequent acid leaching dissolved the embedded ZnO, yielding a hierarchically porous carbon (USV-PET). To quantify the process dynamics, we monitored the compressive load in real time (Figure 1b). The trace exhibits an abrupt jump at the start due to quick particle compaction and contact stiffening, followed by high-frequency oscillations induced by the horn; the steady decrease demonstrates compact fragmentation and loss of contact stiffness. This mechanical signature is consistent with significant interfacial friction and localized stress concentration, resulting in quick in situ heating and bond scission—as opposed to furnace-based carbonization, which requires external heat and a prolonged dwell time. USV-PET exhibits sufficient structural integrity and low apparent mass to rest on a dandelion (Figure 1c), and its apparent density is 0.92 g cm^{-3} measured by liquid

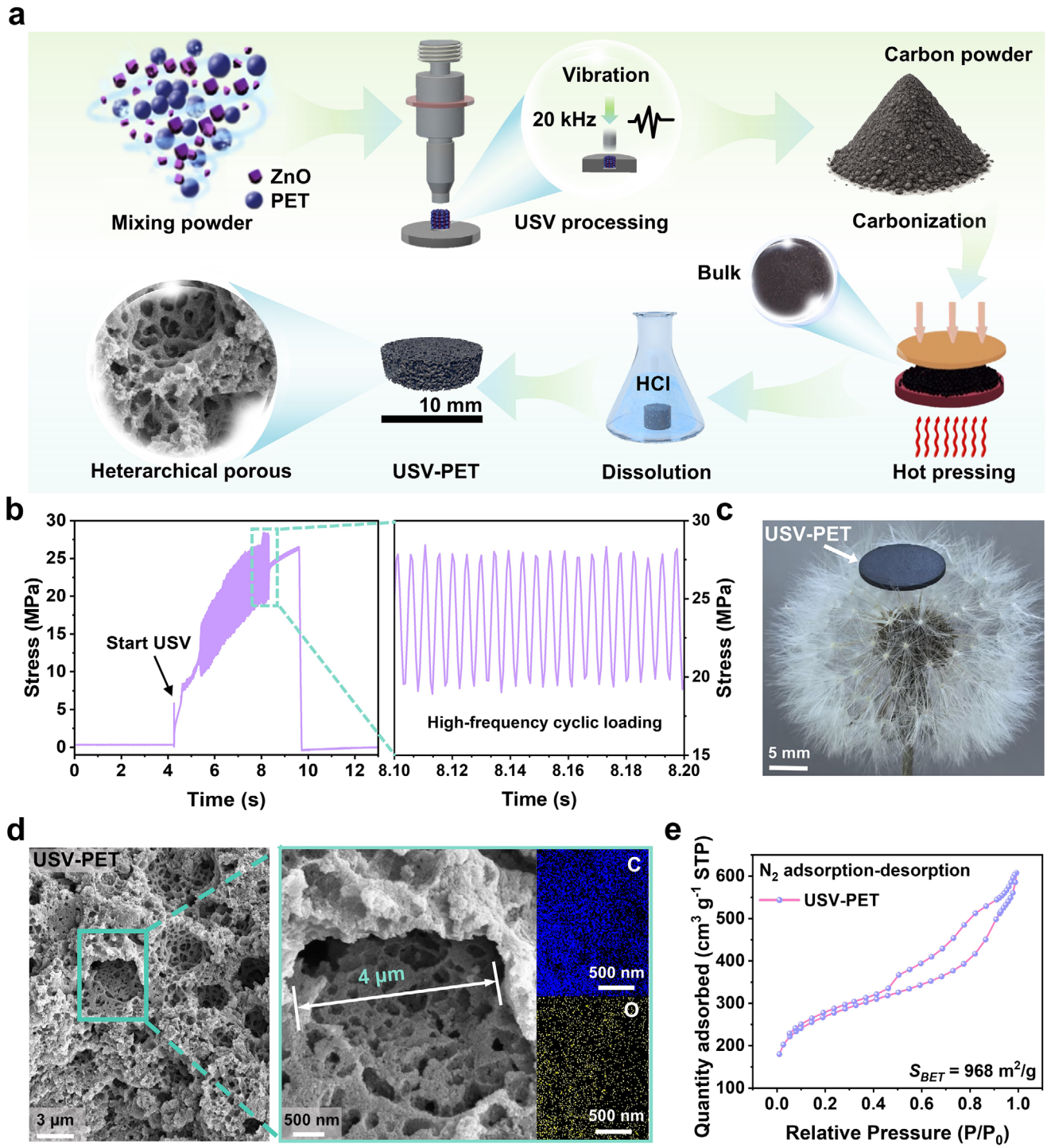

FIGURE 1 | USV converts PET into porous USV-PET. (a) The schematic diagram for preparing USV-PET. (b) The pressure curves for USV treatment of PET/ZnO powder. (c) USV-PET is placed on the dandelion. (d) The SEM images of the micropores and nanopores on USV-PET. (e) The N_2 adsorption and desorption curves of USV-PET.

displacement. Figure 1d reveals an interconnected hierarchical pore network—abundant nanopores decorating micron-sized cavities—arising from the hierarchical effect of ZnO particles (Figure S1). Such architecture facilitates continuous and regulated water transport during solar evaporation [41]. To examine the elemental composition of the final product, energy-dispersive X-ray spectroscopy (EDS) analysis was carried out on USV-PET (Figure 1d). The spectrum revealed that C and O are the dominant elements, while the Zn signal was negligible, indicating that the ZnO template had been almost completely removed during the acid-leaching step. This confirms that the obtained USV-PET consists primarily of a carbon framework, free of significant residual impurities. N_2 adsorption–desorption isotherms (Figure 1e) further confirm the porous nature, giving a BET specific surface area of ~968 m^2 g^{-1} (N_2 probe). The nanopore distribution of USV-PET is provided in Figure S2.

2.2 | Mechanism of "USV Induced Carbonization"

To elucidate how PET transforms under USV, we characterized the samples by X-ray diffraction (XRD), Raman, Fourier-transform infrared (FTIR), and X-ray photoelectron spectroscopy (XPS). Because long-range stacking and ordering are most sensitively captured by X-ray diffraction, we first examined XRD (Figure 2a). PET powder and HP-PET (PET prepared by hot press, see the Experimental Procedures) show nearly identical XRD patterns, where the negligible differences in HP-PET are attributed to hot-pressing-induced texture and densification/thermal-history effects, rather than any crystalline phase transformation [42]. By contrast, the weak diffraction peak at $2\theta = 22.0°$ for USV-PET, which is a broad reflection, characteristic of turbostratic carbon-like (002) stacking ($d_{002} \approx 0.344$ nm), i.e., poorly ordered sp^2 layer packing far from crystalline graphite [43]. To complement stacking information with bond-level chemistry, we next used Raman spectroscopy to probe the sp^2 network (D/G) and to track the persistence or loss of PET-specific vibrations (Figure 2b). Raman spectra of PET and HP-PET exhibit characteristic polymer peaks, including the C═O stretch at 1717 cm^{-1} and C—H stretching modes at 2900 cm^{-1} (sp^3) and ~3050 cm^{-1} (sp^2), confirming that hot pressing preserves the polymer backbone. In stark contrast, USV-PET displays prominent D (1350 cm^{-1}) and G (1580 cm^{-1}) bands with the polymer features largely diminished. The intensity ratio ID/IG = 1.61 indicates a defective sp^2-rich network with a shortened sp^2 correlation length, rather than well-ordered graphite [44]. Together, XRD and Raman establish a coherent picture: hot pressing preserves the polymeric phase, whereas USV converts PET into a disordered, turbostratic sp^2 framework with limited stacking order. FTIR analysis supports the structural development (Figure 2c). PET and HP-PET have significant ester C═O stretching bands (1717–1721 cm^{-1}), C—O (1095 cm^{-1}), and distinctive (C═O)—C vibrations (1249 cm^{-1}), indicating an intact polyester backbone [43]. USV-PET shows a marked attenuation of these ester bands and a more prominent aromatic ν(C═C) near 1600 cm^{-1}. A broad ν(O—H) feature centered around 3200–3600 cm^{-1} is also visible, attributable to surface hydroxyls at edge sites and adsorbed moisture on the porous carbon. To further investigate the changes in carbon-based functional groups before and after treatment, detailed analysis was conducted using XPS carbon spectroscopy. XPS C 1s spectra provide direct evidence of the chemical evolution during USV treatment (Figure 2d–f). The spectra can be deconvoluted into C—C/C═C (284.8 eV), C═O (286.9–287.2 eV), and O—C═O (288.7–288.9 eV) [45]. PET and HP-PET show comparable oxygenated fractions (~35%–37%), consistent with an intact polyester backbone. USV-PET, in contrast, is enriched in C—C/C═C (~86.6%) with a pronounced depletion of carbonyl/carboxyl species (C═O + O—C═O ≈ 8.2%); a small C—OH (~285.6–285.9 eV) component (~5.2%) remains, attributable to edge hydroxyls/adsorbed water and aligned with the broad ν (O—H) band in FTIR (Figure 2c). Elemental analysis (EA) further confirms the compositional evolution: USV-PET exhibits a reduced H content (2.69 ± 0.21 wt.%) and an increased C content (88.23 ± 0.39 wt.%) relative to PET and HP-PET (Figure S3), consistent with carbon enrichment results in Figure 2d–f. These results, in conjunction with the FTIR attenuation of ester bands and the Raman-derived increase in ID/IG, confirm that USV is the primary driver of PET carbonization, triggering rapid chain cleavage, dehydrogenation, and partial aromatization within seconds. Consistently, an FTIR control experiment under identical USV conditions shows that adding ZnO leads to a much stronger attenuation of ester-related bands (ν (C═O) and ν (C—O/C—O—C)) and more pronounced aromatic features (ν (C═C) and ring modes), compared with ZnO-free USV-PET (Figure S4). These results indicate that ZnO plays a synergistic role by providing abundant Lewis-acidic Zn^{2+} sites that coordinate with ester carbonyls, lower the barrier for C—O bond cleavage/β-scission, and thereby accelerate deoxygenation (mainly via decarboxylation), and offering a solid interface/templating effect that helps preserve the emerging porous framework [46, 47]. Together, this synergy facilitates the rearrangement and stabilization of sp^2 clusters, yielding a stable turbostratic sp^2-rich carbon network with substantially reduced oxygen content and improved chemical stability (Figure 2g).

To correlate the spectroscopic evolution with the process parameters, we quantified the temperature transient during ultrasonication using two independent diagnostics (Figure 2h,i). A K-type thermocouple placed at the powder–die contact records a seconds-scale spike to $T_{max} = 534$ K within 0.3 s of vibration onset, followed by rapid relaxation (Figure 2h). Infrared thermography concurrently resolves spatially localized hot spots at the powder surface (Figure 2i), with frames at $t_1 = 3.9$ s and $t_2 = 4.1$ s showing $T_{max} = 340$ and 514 K, respectively. The agreement of the two methods (both on the order of 520 K) indicates that ultrasonication produces brief, localized heating without external heat input, consistent with the rapid chemical changes inferred from XRD/Raman/FTIR/XPS. We note that thermocouple lag and IR emissivity/occlusion can bias absolute values; thus, the reported maxima should be viewed as conservative estimates of the peak local temperature.

To benchmark the efficiency of our USV-assisted strategy, we compared its operating window with conventional carbonization approaches (Figure 2j). Traditional catalytic pyrolytic carbonization (CPC) typically requires elevated temperatures above 700 K and prolonged durations on the order of 10^3–10^4 s, while hydrothermal carbonization (HTC) proceeds at milder temperatures (450–600 K) but over excessively long reaction times (>10^3 s) [48, 49]. Flash Joule heating (FJH), in contrast, achieves carbonization within 60 s, yet demands extreme temperatures exceeding 2000 K and sophisticated electrical setups, which hinder practical scalability [50]. Notably, our method achieves complete carbonization within just a few seconds at ~530 K—combining the kinetic advantages of FJH with the mild conditions of HTC, yet without the high energy penalty of either. This unique position in the time–temperature landscape underscores the unprecedented efficiency and practicality of USV as a low-energy, rapid route to carbon frameworks from waste PET. A detailed comparison of processing conditions across these methods is summarized in Table S1. To further validate the practical applicability of the USV technique, we conducted verification tests on real-world waste plastic feedstocks (predominantly PET-based, encompassing flakes, tubes, films, and sheets), as depicted in Figure S5. XRD characterization results demonstrate that all the aforementioned real waste plastics undergo pronounced carbonization upon USV treatment (Figure S6). The energy input of the USV route was further normalized by the mass of PET processed. Under the experimentally validated condition, ultrasonic treatment at 1.2 kW for 60 s corresponds to 72 kJ per

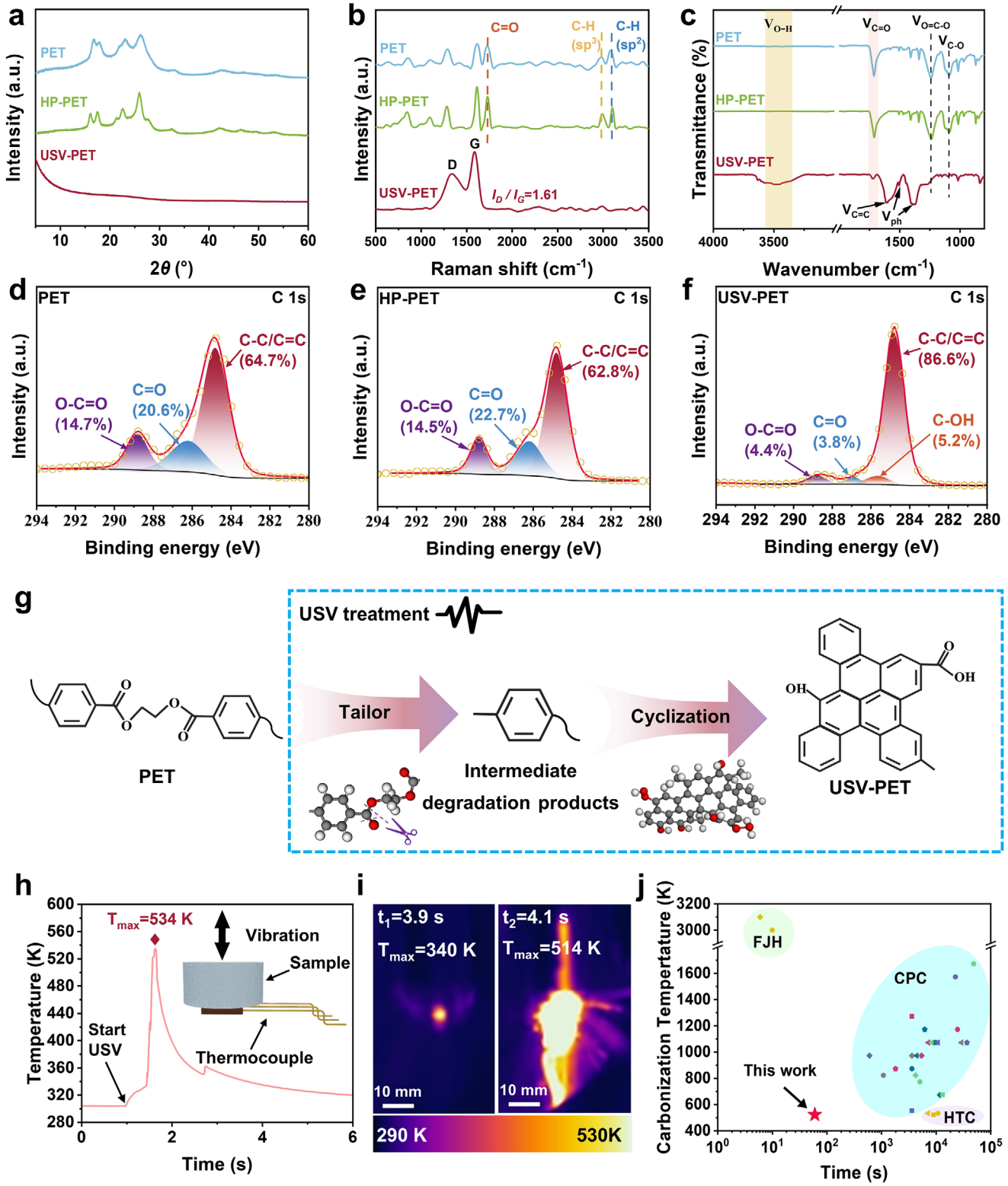

FIGURE 2 | Mechanism characterization of USV-ZnO synergistic carbonization. (a) XRD patterns, and (b) Raman spectra of PET, HP-PET, and USV-PET. (c) FTIR curves of PET, HP-PET, and USV-PET. (d–f) High-resolution C 1s XPS spectra of PET, HP-PET, and USV-PET. (g) Mechanism of the "carbonization" of PET using USV. (h) The temperature curves for USV treatment of PET/ZnO powder. (i) Infrared thermal images of USV processing. (j) Carbonization temperature–time map of PET under USV and other methods.

batch, or 14.4 MJ kg^{-1} PET for the core conversion step. This value is lower than or comparable to representative PET/plastic upcycling processes reported in the literature, including chemical upcycling, 20–60 MJ kg^{-1}; thermal pyrolysis, 20.6 MJ kg^{-1}; flash Joule heating, 23 MJ kg^{-1}; methanolysis, 37–46 MJ kg^{-1}; carbonylolysis, 20.9-22.9 MJ kg^{-1}; and conventional hydrolysis, up to 51 MJ kg^{-1} [18, 51]. These comparisons suggest that the USV strategy offers a relatively low conversion-specific energy input for PET-to-carbon conversion while avoiding prolonged external furnace heating. Collectively, these findings corroborate the preliminary feasibility of extending this proposed strategy toward the efficient treatment of practical PET waste streams.

2.3 | The Photothermal Performance

Due to the turbostratic, sp^2-rich framework established and a rich porous structure, upcycled USV-PET exhibits broadband light absorption and highly efficient photothermal conversion. Its optical properties were quantified using an integrating sphere to measure reflectance (R) and transmittance (T), from which the absorptance was derived as $A(\lambda) = 1 - R(\lambda) - T(\lambda)$. The hierarchically porous architecture promotes multiple scattering and photon trapping (Figure 3a), ensuring efficient solar harvesting across the spectrum. As shown in Figure 3b, USV-PET achieves an average absorptance of 95.7% in the 250–2500 nm range, significantly higher than HP-PET (48.3%). Beyond the structural contribution, this broadband absorption is intrinsically linked to molecular reorganization under USV and ZnO catalysis, which drive dehydrogenation and deoxygenation to yield sp^2-enriched carbon domains with extended conjugation. The increased C═C/C—C fraction revealed by XPS and the pronounced D/G features in Raman confirm the formation of conjugated networks (Figure 2b,d–f), which enables enhanced π-electron delocalization and broadens the absorption window [52, 53]. The synergy of hierarchical architecture and conjugated electronic structure maximizes light–matter interactions, thereby underpinning the superior photothermal response of USV-PET.

Under dry conditions and 1 sun (1 kW m^{-2}), the surface temperature of USV-PET rises rapidly from 304 to 345 K within 8 min. Under the same conditions, HP-PET and the blank substrate show only modest heating, ending at 311 and 308 K, respectively. (Figure 3c). As confirmed by broadband absorption (Figure 3b) and 1 sun–simulated heating tests (Figure 3c), USV-PET exhibits efficient solar-to-thermal conversion. To further resolve its wavelength-dependent photothermal behavior, we employed individual lasers with distinct wavelengths and tunable power densities to systematically evaluate its photothermal response. The experimental setup diagram is shown in the supplementary materials (Figure S7). To assess spectral responsiveness and cycling stability, USV-PET was irradiated at 0.1 W cm^{-2} with lasers of 405, 532, 655, and 1064 nm for 50 min in an on/off cycling protocol. The temperature traces and infrared thermographs (Figure 3d) reveal a sub-15-s rise time and retain this performance without significant loss. At identical power density, shorter wavelengths (e.g., 405 and 532 nm) yield higher heating rates than longer wavelengths, consistent with the measured spectral absorptance (Figure 3e). Given that the near-infrared spectrum constitutes a significant portion of solar energy, we employed an 808 nm laser as a representative source to probe the power-scalable heating crucial for applications like distillation. Under 808 nm irradiation, stepwise increases in power density from 0.1 to 0.5 W cm^{-2} produce fast and fully reversible temperature swings with amplitudes set by power (Figure 3f, left). The heating rate—defined as the initial slope of the temperature rise after laser on—increases approximately linearly with power density over this range, reaching 5 K s^{-1} at 0.5 W cm^{-2} (Figure 3f, right). Collectively, USV-PET combines broadband absorption with rapid, power-scalable heating and excellent cycling stability, pointing to applications in photothermal actuation, solar steam generation, and thermal imaging. Given the dual crises of plastic pollution and freshwater scarcity, we selected interfacial solar evaporation for rigorous application-level validation and further test performance metrics, including broadband absorption, wetting, and salt management.

2.4 | Hydrophilicity and Salt Resistance

High vapor flux in solar steam generators is primarily determined by a continuous water supply to the evaporating interface, and surface wettability is the essential factor that makes this function possible [54]. As shown in Figure 4a, when a water droplet contacts USV-PET, it spreads and is completely imbibed within 1.5 s, evidencing superhydrophilicity and strong capillary wicking. This superhydrophilicity arises from the synergistic effect of hydrophilic surface groups and the interconnected porous structure created after ZnO removal, which together promote rapid wetting and capillary water infiltration. Consistently, water-contact-angle measurements show markedly enhanced wetting for the porous block compared with the dense block prior to ZnO removal (Video S1).

Because salt accumulation within pores can deteriorate evaporation performance, we further evaluated the salt-management capability of USV-PET. A layer of salt crystals was placed on the top surface to emulate interfacial salt deposition during operation (Figure 4b). After 40 min, most surface salt had dissolved and disappeared, attributable to the interconnected hierarchical pores that continuously deliver water to the interface while providing lateral pathways for brine redistribution, thereby dissolving and carrying away salts without clogging. These attributes—instantaneous wetting and capillary-driven brine transport—are essential for maintaining a high evaporation rate and long-term stability in operation [55]. Figure 4c illustrates the passage of salt ions through the evaporator and provides a deeper insight into the mechanism of salt resistance. The evaporation of water at the upper surface of the evaporator increases the concentration and density of ions at the surface, resulting in ion concentration and density gradients. The gradient effect causes salt ions to diffuse from places of high concentration to areas of low concentration. The porous structure within the evaporator creates continuous channels that allow salt ions to diffuse into the bulk water. As a result, a dynamic balance is established between upward water transport and downward ionic diffusion, suppressing surface crystallization. This self-regulating ionic transport ensures long-term salt resistance—an essential prerequisite for stable, high-flux solar evaporation [54].

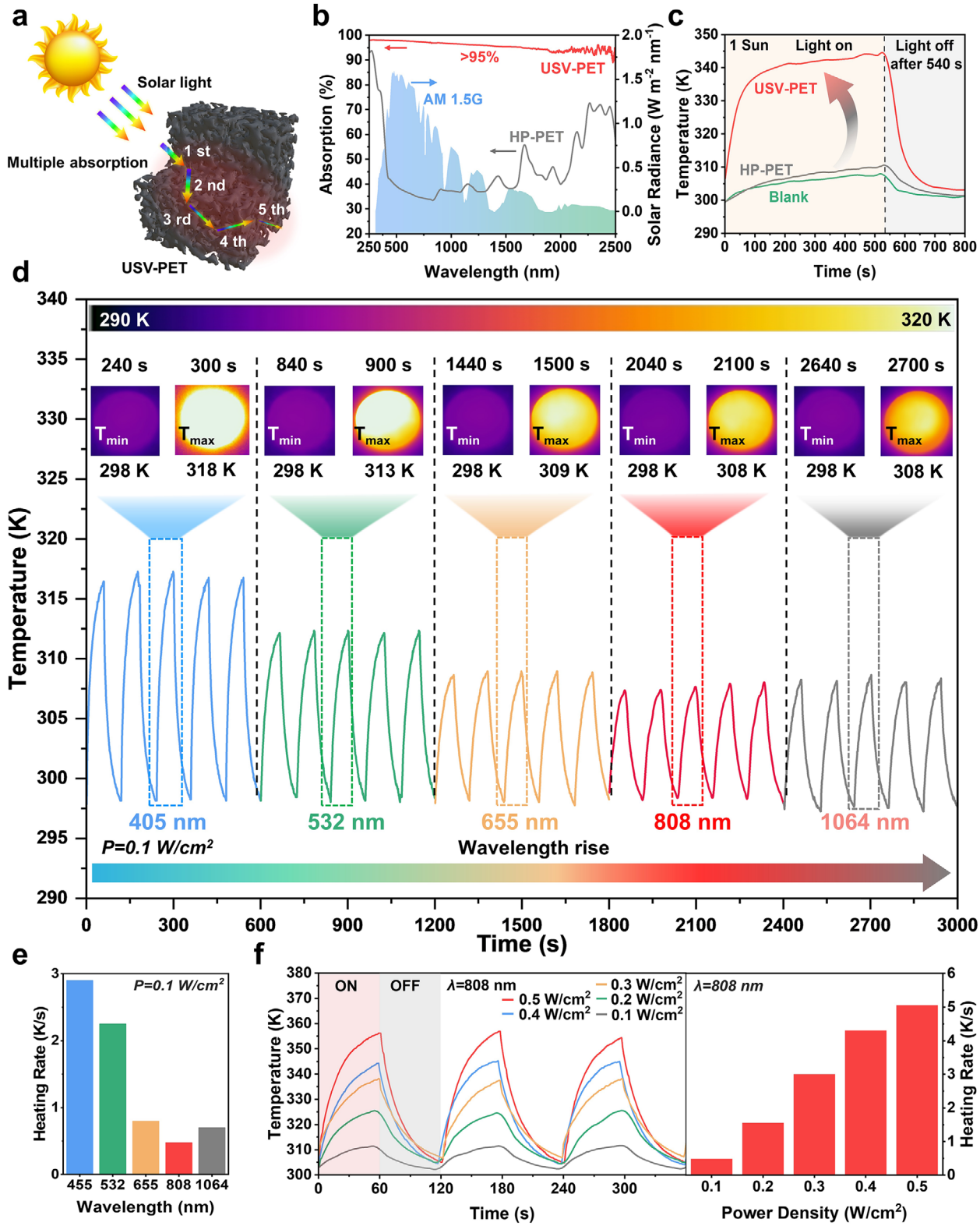

FIGURE 3 | Broadband absorption enables rapid, power-scaled photothermal heating. (a) The absorption mechanism of USV-PET. (b) Absorption spectra of the HP-PET and USV-PET. (c) Surface temperature curves of Blank, HP-PET, and USV-PET under 1 kW m^{-2} irradiation. (d) The temperature rise curve of USV-PET under different wavelength irradiation at a power density of 0.1 W cm^{-2} and Infrared images. (e) The heating rate of USV-PET irradiated with different wavelength irradiation at a power density of 0.1 W cm^{-2}. (f) Temperature rise curve of USV-PET under different power irradiation with an 808 nm laser and the heating rate of USV-PET irradiated with 808 nm laser with different energy power.

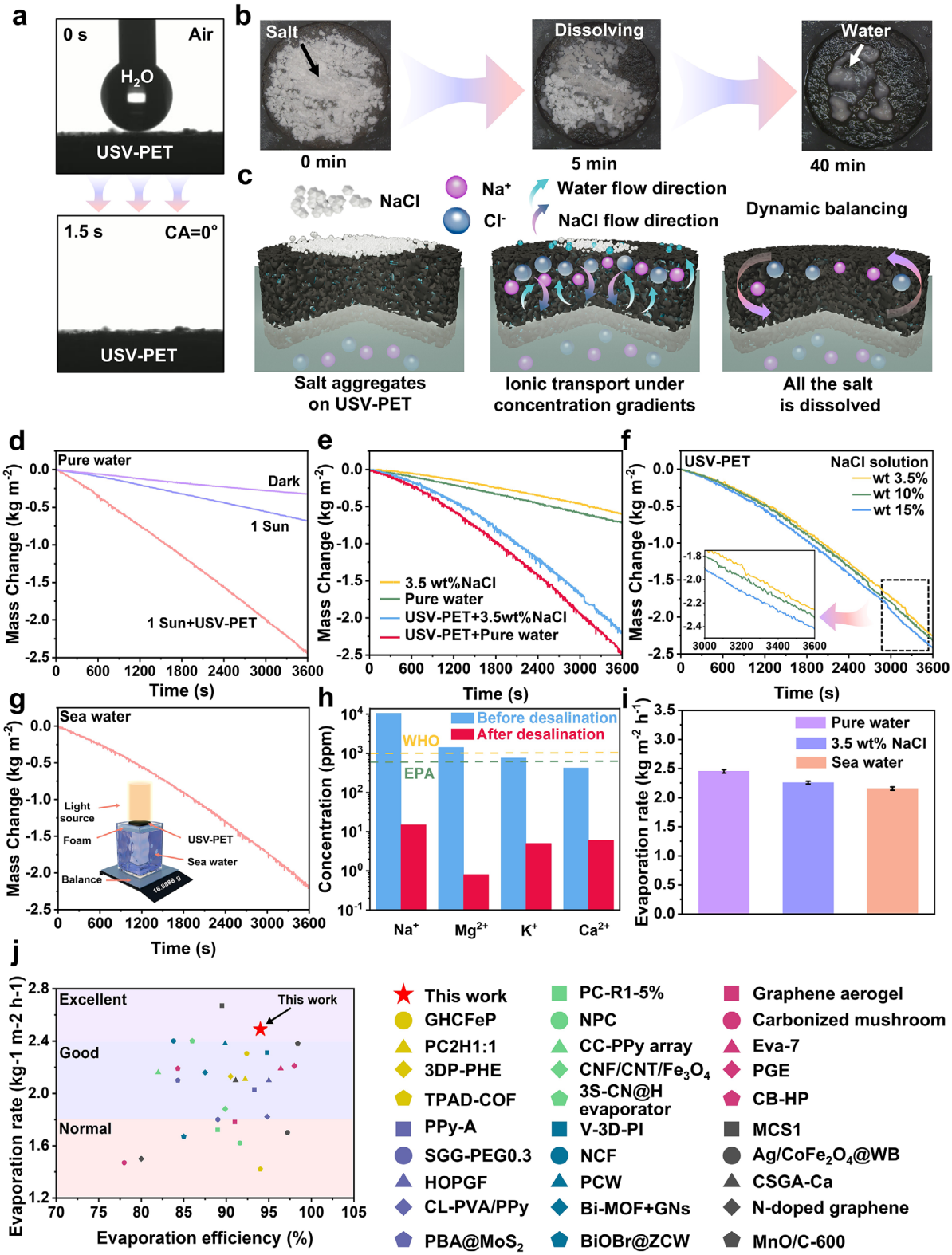

FIGURE 4 | Instantaneous wetting and high salt tolerance support high-throughput distillation. (a) The evolution of the water angle on USV-PET. (b) Optical photograph of USV-PET surface simulating dissolution changes of accumulated salt. (c) A graphic depicting the salt and water transport mechanisms. (d) Cumulative water mass change versus irradiation time under one solar irradiation. (e) Evaporation performance of simulated seawater and pure water under 1 sun. (f) Mass change of NaCl solution of wt 3.5/10/15% over time of USV-PET. (g) Solar-driven evaporation of real seawater and a schematic diagram of the evaporation unit. (h) The measured concentrations of Na^+, Mg^{2+}, K^+, and Ca^{2+} in an actual seawater sample from the Yellow Sea before and after distillation, the dashed lines represent the WHO and EPA standards. (i) Stability of USV-PET in solar-driven steam generation. (j) The comparison of the evaporation efficiency and evaporation rate of the previous materials.

2.5 | Evaporation Performance of USV-PET

Motivated by the broadband photothermal response, superhydrophilicity, and salt resistance of USV-PET, we investigated its solar steam–generation performance. Under simulated solar irradiation at 1 sun, USV-PET delivers a steady evaporation rate of 2.49 kg m^{-2} h^{-1}, which is 3.7× that of pure water (0.67 kg m^{-2} h^{-1}) (Figure 4d). The enhancement stems from the higher surface temperature achieved by the USV-PET evaporator relative to bare water under the same irradiation, which accelerates vapor escape from the interface. USV-PET exhibits an evaporation rate of 2.12 kg m^{-2} h^{-1} even after subtracting the dark evaporation contribution. Importantly, the equivalent evaporation enthalpy (E_{equ}) of USV-PET was also determined by subtracting the dark evaporation contribution. The enthalpy of USV-PET is calculated by Equation (1):

$$U_{in} = E_{equ}\, m_g = E_0\, m_0 \tag{1}$$

where U_{in} is the total energy absorbed from the environment per hour; E_0 and m_0 refer to the water evaporation enthalpy (kJ g^{-1}) and the mass loss (g) of water in 1 h without USV-PET in the dark, respectively; m_g is the water mass change using USV-PET. To measure the water evaporation enthalpy, a control experiment was conducted to assess water loss in the dark over 1 h (Figure S8). The calculated E_{equ} is 1614 J g^{-1}, which is markedly lower than the theoretical enthalpy of bulk water (2434 J g^{-1}). This reduction indicates that USV-PET not only raises the interfacial temperature but also effectively lowers the energetic barrier for phase change. The corresponding photothermal conversion efficiency was calculated to be 95% (Note S1). To further validate the strong salt tolerance of USV-PET, evaporation tests were conducted with saline feeds of varying concentrations. Even when using a highly concentrated 15 wt.% NaCl solution, the evaporation rate (2.42 kg m^{-2} h^{-1}) remains nearly identical to that obtained with a 3.5 wt.% solution. This result demonstrates that USV-PET maintains stable performance under hypersaline conditions (Figure 4f). The decreased concentration gradient between the saltwater at the bottom and the saltwater at the top of the evaporator, which slows down the rate of water transport, is the main cause of the modest decrease in rate [53]. The application of USV-PET for the distillation and purification of wastewater is crucial in addressing real-world water scarcity due to uneven distribution of water resources, with seawater occupying the majority of resources and pollution from energy development [56].

2.6 | Distillation Performance, Durability, and Scalability of USV-PET

To validate the practical distillation capability, USV-PET was further evaluated using real seawater collected from the Yellow Sea (Figure 4g). Under one-sun illumination, the evaporator achieved a stable evaporation rate of 2.19 kg m^{-2} h^{-1}, accompanied by continuous and nearly linear mass loss, indicating efficient and steady photothermal-driven water evaporation in natural saline conditions. No visible salt accumulation occurred on the surface throughout the process, highlighting the excellent salt-rejection ability of USV-PET during actual seawater distillation. The Na^+, K^+, Mg^{2+}, and Ca^{2+} concentrations of condensed water range from ca. 400–11000 ppm to ca. 0.8–15 ppm (Figure 4h). These values are well below the World Health Organization (WHO) and U.S. Environmental Protection Agency (EPA) recommended limits for total dissolved solids (TDS) in drinking water—approximately 1000 ppm (WHO) and 500 ppm (EPA)—demonstrating the excellent distillation performance of USV-PET under real-world conditions. To probe durability, evaporation tests were conducted under one-sun using pure water, 3.5 wt.% NaCl brine, and natural seawater; the mean evaporation rates were 2.45 ± 0.028, 2.26 ± 0.023, and 2.15 ± 0.030 kg m^{-2} h^{-1}, respectively, and no performance loss was observed over 10 reuse cycles, demonstrating excellent robustness (Figure 4i). To assess the evaporation stability and scalability under variable solar intensities, we further performed tests under simulated irradiances of 0.5, 1, 1.5, 2, and 3 suns. As shown in Figure S9, the evaporation rate increases monotonically with rising power density, while the evaporation curve maintains a smooth shape without abrupt fluctuations. Furthermore, under identical testing conditions, USV-PET exhibited a higher evaporation rate (2.41 kg m^{-2} h^{-1}) than the representative commercial carbon materials, including graphene (1.23 kg m^{-2} h^{-1}), activated carbon (1.37 kg m^{-2} h^{-1}), porous carbon fiber (1.41 kg m^{-2} h^{-1}), and carbon nanotube (1.55 kg m^{-2} h^{-1}) (Figure S10). Compared with metallic, carbon-based, and hydrogel photothermal materials, USV-PET achieves a distinctly higher evaporation rate and competitive efficiency (Figure 4j). The evaporation rates and conversion efficiencies of these samples are listed in Table S2. We further evaluated fabrication cost, evaluated durability, and environmental robustness relevant to practical deployment. A preliminary lab-scale cost analysis for a single batch of five USV-PET discs is summarized in Table S3. To evaluate its resistance to harsh environments, USV-PET was immersed in 1 M Hydrochloric acid (HCl) and 1 M NaOH solutions for 48 h. The porous morphology remained intact (Figure S11), and the seawater evaporation rate remained stable (Figure S12). Beyond operational robustness, reproducibility across fabrication cycles is also essential for real-world deployment. USV-PET samples prepared in five independent batches under identical conditions exhibited comparable porous morphologies in SEM (Figure S13), consistent carbonization characteristics with a carbon content of 88.6 ± 1.8 wt.%, and nearly overlapping seawater evaporation performance (Figure S14).

2.7 | Outdoor Solar Seawater Distillation Application

To demonstrate the scalable and programmable manufacturability of USV-PET, monolithic blocks and discs with diverse geometries were fabricated. Curved samples were produced by hot-pressing at 540 K under 50 MPa using molds with a contour radius of 0.5 mm, yielding mechanically robust curved monoliths. Flat USV-PET membranes were further shaped through binder-free vacuum filtration into circular discs with diameters up to 5 cm, exhibiting uniform thickness and smooth surfaces. In addition, size-programmable pieces ranging from 1.5 to 6 cm in diameter were obtained by coating method, confirming the excellent form-factor versatility of USV-PET (Figure 5a) (specific coating procedure steps are detailed in the Supporting Information). These results highlight the material's potential for scalable integration into solar-steam devices of various configurations and dimensions. Furthermore, to validate solar steam generation

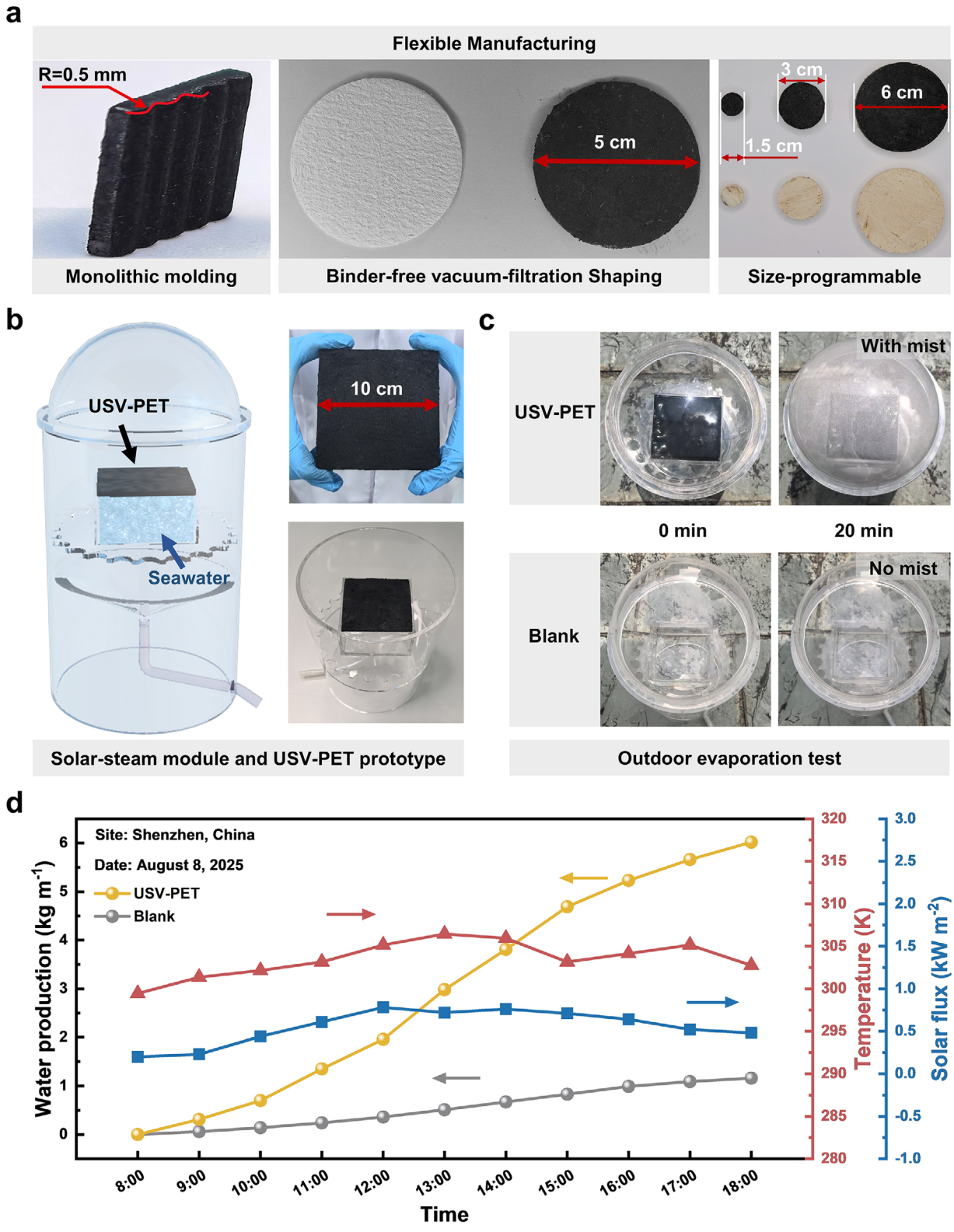

FIGURE 5 | Scalable USV-PET modules yield outdoor freshwater—waste to wealth. (a) Scalable fabrication and programmable shaping of USV-PET monoliths. (b) Schematic and prototype of the solar-steam generation module. (c) Photographs of outdoor evaporation test with USV-PET and blank conditions. (d) Outdoor solar-evaporation performance of USV-PET and blank under natural sunlight.

under real sunlight at Shenzhen University in Shenzhen, China (22.53°N, 113.94°E, Figure S15), we constructed a bench-scale distillation system comprising an evaporation chamber, a 10 cm × 10 cm USV-PET-coated wood evaporator, a condenser, and a collection reservoir. A transparent PMMA cover promoted vapor condensation and directed the condensate to the outlet (Figure 5b). Under natural sunlight, rapid vapor generation was visually confirmed: as shown in Figure 5c, fine water droplets formed on the inner surface of the cover within 20 min for the USV-PET device, whereas the blank control (without USV-PET) exhibited no visible condensation, confirming the strong photothermal and water-supply capability of USV-PET. Continuous evaporation was observed in the mass change of water over a 10-h period (8:00–18:00, August, 2025, Shenzhen, China) (Figure 5d). The solar flux increased from 0.20 kW m^{-2} at 08:00 to 0.78 kW m^{-2} at noon, remained 0.71–0.78 kW m^{-2} from 12:00–15:00, and decreased to 0.53 kW m^{-2} by 18:00. Ambient temperature varied between 299–308 K, peaking at around 13:00. USV-PET module steadily increased from 0 to 6.02 kg m^{-2} by 18:00, whereas the blank reached only 1.16 kg m^{-2}, delivering an overall ~5.2× higher yield. The gap emerged early (09:00: 0.31 vs 0.06 kg m^{-2}) and continued to widen through noon when the solar flux peaked (0.71–0.78 kW m^{-2}), evidencing sustained interfacial evaporation and efficient water supply with USV-PET. For completeness, we provide hour-by-hour net evaporation rates in the Supplementary Information (Figure S16). Based on field data, a 1 m^2 USV-PET module can cover the daily freshwater demands of approximately three individuals. Importantly, the evaporator is made by upcycling waste PET into a strong, scalable photothermal monolith, demonstrating a circular-economy pathway that turns discarded polymers. To further assess longer-term operational durability, we conducted a 20-day outdoor experiment (Figure S17). The daily collected water output remained stable without noticeable performance decay. These results highlight the durability and environmental tolerance of USV-PET in realistic settings.

3 | Conclusion

We introduce a field-driven, seconds-scale carbonization of post-consumer PET, powered by high-frequency USV, transforming a technique traditionally used for polymer welding into an upcycling process that directly drives polymer-to-carbon conversion. Requiring no external thermal input and triggering rapid chain scission, deoxygenation, and aromatization to yield porous, device-ready carbons. The resulting carbons exhibit exceptional hydrophilicity and photothermal conversion, achieving a solar steam generation rate of 2.49 kg m^{-2} h^{-1} with 95% efficiency under one sun, demonstrated in both seawater distillation and outdoor tests. Scalable shaping via hot pressing, coating, and binder-free filtration underscores the practicality of manufacturing. More broadly, this work redefines plastic waste as a renewable carbon feedstock, establishing a practical "turning waste into wealth" paradigm for clean-water production within a circular-economy framework. A key open question now is how acoustic parameters—frequency, amplitude, and impedance matching—can be generalized across polymer chemistries to program pore architecture and conductivity at scale, thereby defining a broader playbook for low-energy carbon manufacturing.

4 | Experimental Procedures

4.1 | Materials Preparation

PET was used as the carbon precursor. PET (98%) powder with an average particle size of ~100 μm was purchased from Hengli New Materials, Zhangmutou, Dongguan, China. The original morphology of PET powder is provided in the Supporting Information (Figure S18). Waste PET beverage bottles were collected from a local supermarket (Shenzhen). PET plastic tubes were purchased from Dongguan Yuwei Insulation Materials Co., Ltd., China. PET plastic sheets were purchased from Dongguan Youhuang Plastic Co., Ltd., China. PET plastic film was purchased from Dongguan Chang'an Tianfu Plastic Materials Trading Department. ZnO powder (99.99%) was obtained from Qinghe Xindun Metal Materials Co., Ltd. (China), and sodium chloride (NaCl, 98%) from Maclean Biochemical Technology Co., Ltd. in Shanghai. Pine block was supplied by Shuyang Lvjiyuan Wood Products Company (China). Seawater was collected from the Yellow Sea (locally known as Huanghai Sea, China). HCl (1 M), sodium hydroxide (NaOH, 1 M), chitosan (99%), and acetic acid (CH_3COOH, 99.8%) were supplied by Sinopharm Chemical Reagent Company (China). Ammonia solution (5%) was purchased from Yuan Shi Standard Materials (Quanzhou) Technology Co., Ltd. Unless otherwise stated, PET and ZnO were mixed at a 1:1 mass ratio using a powder blender to yield a homogeneous mixture (no milling media). This mass ratio affords abundant hierarchical porosity and nearly optimal PET conversion, while further increased ZnO mass induces negligible performance enhancement [46, 47].

4.2 | USV Process

The USV apparatus consisted of a piezoelectric transducer, a booster, a sonotrode (horn), and a control unit for parameter tuning. An AC signal was converted by the transducer into a 20 kHz vibration and amplified to a peak amplitude of 44.4 μm, which was transmitted to the sample through the horn. During USV, the horn was pneumatically preloaded at 400 kPa and brought into direct contact with the PET or PET/ZnO powder bed. USV was triggered when an axial load of 100 N was applied; the horn then operated at 20 kHz with 100% amplitude (44.4 μm). A 304 stainless-steel die confined the powders in a 10 mm diameter through-hole, after which ultrasonication was applied in repeated bursts, each lasting 6 s, for a total of ten cycles. In this process, energy was delivered into the powder bed to induce the carbonization of PET. During the process, a homemade force gauge was used to monitor pressure in real-time. The data was then processed and transferred to a computer using a National Instruments NI-9237 data collection card with a sampling frequency of 1 kHz. Temperature was measured by two complementary methods: (i) a K-type thermocouple embedded at the die-powder interface, sampled at 100 Hz via the NI-9237 (temperature accuracy = 0.2 K); and (ii) surface temperature was recorded continuously at 12 Hz using an infrared camera (Fotric 280D, China) during the USV burst to capture spatiotemporal heating. All signals were time-stamped and logged to a computer for subsequent analysis.

4.3 | Preparation of HP-PET and USV-PET

4.3.1 | HP-PET

Unlike the default premixing protocol, HP-PET was prepared from neat PET only (no ZnO) and without USV treatment, serving as a thermal-processing control. For each specimen, ∼0.12 g of dried PET powder was loaded into a tungsten steel cylindrical mold (inner diameter = 10 mm). Hot pressing was performed in ambient air using a hydraulic press: the temperature was ramped at 10 K min^{-1} to 540 K, followed by a 20 min dwell under a uniaxial pressure of 50 MPa. After the dwell, the sample was cooled under load at ∼5 K min^{-1} to < 333 K, then demolded and allowed to equilibrate to room temperature. The resulting HP-PET was obtained as a cylindrical disc (10 mm in diameter and ∼1 mm in thickness).

4.3.2 | Preparation of USV-PET

0.50 g of the mixed powder was placed into a die cavity with a diameter of 10 mm. Following the USV-assisted carbonization procedure detailed in Section 4.2, the carbonized product was collected, yielding a recovered mass of approximately 0.39–0.40 g per batch. This corresponds to a mass recovery rate of 79.2 ± 2.6%, with the mass-recovery workflow illustrated in Figure S19. The as-collected carbonized powder was then subjected to subsequent hot pressing and leaching treatments (with scale-up potential through increased contact area, Figure S20). Then, the carbonized powder (∼0.08 g each) was loaded into a tungsten steel cylindrical mold (inner diameter = 10 mm) and hot-pressed using the same thermo-mechanical profile as HP-PET. To remove Zn species, five hot-pressed USV-PET discs were immersed in 10 mL of 1 M HCl at room temperature for 2 h. The solids were collected by vacuum filtration, washed three times with deionized water, and dried at room temperature for 6 h. ICP analysis showed a residual Zn content of 0.231 ± 0.005 wt.% in the leached USV-PET.

4.4 | Recovery and Regeneration of ZnO

The Zn-containing acidic filtrates collected after leaching were combined from 10 batches and treated with 5 wt.% ammonia solution to precipitate zinc hydroxide. The precipitate was separated, dried, and calcined to regenerate ZnO (schematic illustration of ZnO recycling, Figure S21). The recovered ZnO exhibited a stable recovery ratio of 85.1 ± 1.5% over five cycles. XRD patterns of the regenerated and original ZnO were nearly identical, confirming preservation of the ZnO crystalline phase and its recyclability for subsequent use (Figure S22). The remaining supernatant was neutralized and handled according to standard laboratory wastewater protocols.

4.5 | Characterization of Multi-Scale Structures

N_2 adsorption–desorption isotherms were measured at 77 K on a Micromeritics ASAP 2020, and specific surface areas were calculated by the BET method. The morphologies of PET, ZnO, and USV-PET were examined by scanning electron microscopy (SEM; Fei Quanta FEG 450). Elemental distributions were analyzed by SEM equipped with EDS. XRD patterns were collected on a Rigaku MiniFlex 600 with Cu Kα radiation over 2θ = 5–60° at 5° min^{-1}. FTIR spectra were recorded on a Nicolet iN10 spectrometer. Raman spectra were acquired on a WITec alpha300R. XPS (Thermo Scientific K-Alpha) was used to analyze surface elemental composition and chemical states. Inductively coupled plasma optical emission spectroscopy (ICP-OES) was performed on an Agilent 5800 instrument (USA) to quantify the Zn in both solids and liquids. EA (CHNS and O modes) was conducted using an Elementar vario EL cube (Germany) to quantify C/H/N/S/O contents of samples. Optical transmittance (T), reflectance (R), and absorptance (A) were measured using an integrating-sphere UV–Vis–NIR spectrophotometer (Shimadzu UV-3600); A was obtained as Equation (2):

$$A(\lambda) = 1 - R(\lambda) - T(\lambda) \tag{2}$$

The temperature evolution of HP-PET, and USV-PET was monitored in real time with an infrared thermal imager (Fotric 280d). The concentrations of Na^+, K^+, Ca^{2+}, and Mg^{2+} were determined by inductively coupled plasma–optical emission spectroscopy (ICP-OES). Static water contact angles (CA) were measured with a drop-shape analyzer (DSA100S, Krüss Germany) with a 1 μL water droplet.

4.6 | Photothermal Characterization

To evaluate the photothermal conversion of USV-PET, samples mounted on quartz substrates were irradiated with an 808 nm laser at varied power densities. Surface temperature was recorded continuously at 1 Hz with an infrared camera (Fotric 280D, China). In addition, a multi-wavelength test was conducted using lasers at 405 nm (PGL-V-H-405), 532 nm (PGL-V-H-532), 655 nm (PGL-V-H-655), 808 nm (PGL-V-H-808), and 1064 nm (PGL-V-H-1064); the beam was switched every 60 s, and each wavelength irradiated the sample for 600 s (total 3000 s). The 808 nm source was a 5 W fiber-coupled multimode diode laser; in the multi-wavelength protocol, the sample was irradiated normal to the surface.

4.7 | Water-Evaporation Tests

A xenon lamp equipped with an AM 1.5G filter (CEL-HXF-300, Beijing Education Jinguang Co.) was used to simulate sunlight at 1 sun (1 kW m^{-2}). The irradiance was monitored with a power meter (CEL-NP2000), the surface temperature was tracked by an infrared thermal imager, and mass loss was continuously recorded by a Sartorius Quintix35-1CN analytical balance (readability 0.01 mg) connected to a computer. During testing, USV-PET was seated on a foam wicking reservoir so that water permeated from the bottom and sides to the USV-PET surface; the lamp was then switched on and set to 1 sun. To suppress parasitic evaporation from the container and foam, the glass bottle and all foam except the exposed USV-PET area were wrapped with aluminum foil, ensuring that only the sample surface received illumination. Ambient conditions were controlled at 299 K and 65% relative humidity for all measurements. Subsequently, we calculated the evaporation rate (m', kg m^{-2} h^{-1}), conversion efficiency (η, %), and enhancement factor (*E.F.*) by using the

following Equations (3)–(5) [57]:

$$m' = \frac{\Delta m}{S \times t} \tag{3}$$

$$\eta = m' \times \frac{h_{Lv}}{3600 \times P_{in}} \tag{4}$$

$$E.F. = \frac{m(absorber)}{m(blank)} \tag{5}$$

where Δm represents water mass reduction in 1 h (kg), S represents evaporator area (m^2), m' stands for evaporation rate under irradiation after subtracting dark evaporation rate (kg m^{-2} h^{-1}), t stands for irradiation time (i.e., 1 h), h_{Lv} represents the latent heat of water vaporization (J g^{-1}), and Pin represents solar power (kW m^{-2}). A solar evaporation experiment without evaporators was also conducted and labeled as "Blank".

Author Contributions

Shengyu Zhao: Methodology, Validation, Formal analysis, Investigation, Data curation, Writing – original draft, Writing – review & editing, Visualization. **Shike Huang:** Writing – review & editing. **Kangyu Lin**, **Bangliang Cao**, **Jinbiao Huang**, **Junsheng Liu**, **Xiangyang Yu**, **Jiasen Sun**, **Shuzhe Zhang**, **Chaoqun Pei**, **Wenqing Ruan**, **Xiaodi Liu**, **Boyang Wu**, **Wenzhe Bao** and **Jianan Fu:** Investigation, Methodology, Data Curation, Supervision. **Jiang Ma:** Investigation, Writing – review & editing, Resources, Supervision.

Acknowledgements

The work was financially supported by the Key-Area Research and Development Program of Guangdong Province (Grant No. 2024B0101070001), the NSF of China (Grant Nos. 52571191, 52401217, 52271150, 52571190), the Science, Technology and Innovation Commission of Shenzhen Municipality (Grants Nos. RCJC20221008092730037, JCYJ20250604182240052, JCYJ20240813141413018). We thank the Instrumental Analysis Center of Shenzhen University for the assistance with the Electron Microscope.

Conflicts of Interest

The authors declare no conflicts of interest.

Data Availability Statement

The authors confirm that the data supporting the findings of this study are available within the article and its supplementary materials.

References

1. "On the Plastics Crisis," *Nature Sustainability* 6 (2023): 1137, https://doi.org/10.1038/s41893-023-01236-z.

2. K. P. Sullivan, A. Z. Werner, K. J. Ramirez, et al., "Mixed Plastics Waste Valorization through Tandem Chemical Oxidation and Biological Funneling," *Science* 378 (2022): 207–211, https://doi.org/10.1126/science.abo4626.

3. L. Cabernard, S. Pfister, C. Oberschelp, and S. Hellweg, "Growing Environmental Footprint of Plastics Driven by Coal Combustion," *Nature Sustainability* 5 (2022): 139–148, https://doi.org/10.1038/s41893-021-00807-2.

4. A. S. Pottinger, R. Geyer, N. Biyani, et al., "Pathways to Reduce Global Plastic Waste Mismanagement and Greenhouse Gas Emissions by 2050," *Science* 386 (2024): 1168–1173, https://doi.org/10.1126/science.adr3837.

5. J. Zheng and S. Suh, "Strategies to Reduce the Global Carbon Footprint of Plastics," *Nature Climate Change* 9 (2019): 374–378.

6. J. Cheng, J. Li, R.-G. Xiong, et al., "Potentially Harmful Effects of Micro-/Nanoplastics on Humans as Well as Protective Actions of Dietary Natural Products," *Trends in Food Science & Technology* 156 (2025): 104841, https://doi.org/10.1016/j.tifs.2024.104841.

7. R. C. Thompson, W. Courtene-Jones, J. Boucher, S. Pahl, K. Raubenheimer, and A. A. Koelmans, "Twenty Years of Microplastic Pollution Research—What Have We Learned?," *Science* 386 (2024): adl2746, https://doi.org/10.1126/science.adl2746.

8. X. F. Wei, W. Yang, and M. S. Hedenqvist, "Publisher Correction: Plastic Pollution Amplified by a Warming Climate," *Nature Communications* 15 (2024): 2524, https://doi.org/10.1038/s41467-024-46860-1.

9. P. Stegmann, V. Daioglou, M. Londo, D. P. van Vuuren, and M. Junginger, "Plastic Futures and Their CO_2 Emissions," *Nature* 612 (2022): 272–276.

10. S. H. Joo, "Addressing Climate Change Mitigation: Implications for the Sustainable Alternatives to Plastics," *Cambridge Prisms: Plastics* 2 (2024): 1.

11. K. D. Nixon, Z. O. G. Schyns, Y. Q. Luo, et al., "Analyses of Circular Solutions for Advanced Plastics Waste Recycling," *Nature Chemical Engineering* 1 (2024): 615–626.

12. S. Chen and Y. Hu, "Advancements and Future Directions in Waste Plastics Recycling: From Mechanical Methods to Innovative Chemical Processes," *Chemical Engineering Journal* 493 (2024): 15, https://doi.org/10.1016/j.cej.2024.152727.

13. S. Huang, F. Sun, R. Sun, et al., "Micro- and Nanoscale Glass Compression Molding Using the Metallic Glass Mold," *Journal of Materials Science & Technology* 249 (2026): 230–241, https://doi.org/10.1016/j.jmst.2025.05.073.

14. C. C. Uzosike, L. H. Yee, and R. V. Padilla, "Small-Scale Mechanical Recycling of Solid Thermoplastic Wastes: a Review of PET, PEs, and PP," *Energies* 16 (2023): 1406.

15. Z. Xu, K. Sanchez-Rivera, C. Granger, et al., "Solvent-Based Plastic Recycling Technologies," *Nature Chemical Engineering* 2 (2025): 407–423.

16. H. J. Buck, W. Carton, J. F. Lund, and N. Markusson, "Countries' Long-Term Climate Strategies Fail to Define Residual Emissions," *Nature Climate Change* 13 (2023): 317–319, https://doi.org/10.1038/s41558-023-01614-7.

17. A. Gomez-Sanabria, G. Kiesewetter, Z. Klimont, W. Schoepp, and H. Haberl, "Potential for Future Reductions of Global GHG and Air Pollutants from Circular Waste Management Systems," *Nature Communications* 13 (2022): 106, https://doi.org/10.1038/s41467-021-27624-7.

18. J. Cao, H. Liang, J. Yang, et al., "Depolymerization Mechanisms and Closed-Loop Assessment in Polyester Waste Recycling," *Nature Communications* 15 (2024): 6266, https://doi.org/10.1038/s41467-024-50702-5.

19. R. A. Clark and M. P. Shaver, "Depolymerization within a Circular Plastics System," *Chemical Reviews* 124 (2024): 2617–2650, https://doi.org/10.1021/acs.chemrev.3c00739.

20. A. Schade, M. Melzer, S. Zimmermann, T. Schwarz, K. Stoewe, and H. Kuhn, "Plastic Waste Recycling—A Chemical Recycling Perspective," *ACS Sustainable Chemistry & Engineering* 12 (2024): 12270–12288, https://doi.org/10.1021/acssuschemeng.4c02551.

21. Y. Wu, Q. Hu, Y. Che, and Z. Niu, "Opportunities and Challenges for Plastic Depolymerization by Biomimetic Catalysis," *Chemical Science* 15 (2024): 6200–6217, https://doi.org/10.1039/D4SC00070F.

22. L. Cheng, X. Chen, J. Gu, N. Kobayashi, H. Yuan, and Y. Chen, "Chemical Recycling of Waste Plastics: Current Challenges and Perspectives,"

Fundamental Research 5 (2025): 919–922, https://doi.org/10.1016/j.fmre.2023.12.023.

23. J. Qin, F. Wu, Y. Dou, et al., "Advanced Catalysts for the Chemical Recycling of Plastic Waste," *Advanced Materials* 37 (2025): 2418138, https://doi.org/10.1002/adma.202418138.

24. Z. Zhang, B. Y. Zhang, Q. Tang, et al., "Plastic Upcycling into Advanced Materials," *Advanced Materials Technologies* 11 (2026): 01385, https://doi.org/10.1002/admt.202501385.

25. L. Dai, O. Karakas, Y. Cheng, et al., "A Review on Carbon Materials Production from Plastic Wastes," *Chemical Engineering Journal* 453 (2023): 23.

26. Z. Ma, L. Wang, Z. Wang, et al., "Magnetically Reusable Carbon Nanotube Coated Co-based Catalysts towards Highly Efficient Transfer Hydrogenation of Nitroarenes," *Chemcatchem* 16 (2024): 27.

27. S. Ren, X. Xu, K. Hu, et al., "Salt-Templated Transformation of Waste Plastics into Single-Atom Catalysts for Environmental and Energy Applications," *Nature Communications* 16 (2025): 8194, https://doi.org/10.1038/s41467-025-63648-z.

28. K. Cao, S. Zhang, Y. Shi, X. Diao, R. Wei, and N. Ji, "Catalytic Upgrading of Plastic Wastes into High-Value Carbon Nanomaterials: Synthesis and Applications," *ACS Nano* 19 (2025): 12734–12761, https://doi.org/10.1021/acsnano.5c03391.

29. R. Chakraborty, K. Vilya, M. Pradhan, and A. K. Nayak, "Recent Advancement of Biomass-Derived Porous Carbon Based Materials for Energy and Environmental Remediation Applications," *Journal of Materials Chemistry A* 10 (2022): 6965–7005, https://doi.org/10.1039/D1TA10269A.

30. S. Khan, M. Ul-Islam, M. W. Ahmad, et al., "Synthetic Methodologies and Energy Storage/Conversion Applications of Porous Carbon Nanosheets: a Systematic Review," *Energy & Fuels* 36 (2022): 3420–3442, https://doi.org/10.1021/acs.energyfuels.2c00077.

31. D. K. Sam, H. Li, Y.-T. Xu, and Y. Cao, "Advances in Porous Carbon Materials for a Sustainable Future: a Review," *Advances in Colloid and Interface Science* 333 (2024): 103279.

32. G. Hu, H. Liu, K. Liu, et al., "All-in-one Carbon foam Evaporators for Efficient co-Generation of Freshwater and Electricity," *Advanced Functional Materials* 35 (2025): 12.

33. X. Liu, C. Ma, Y. Wen, et al., "Highly Efficient Conversion of Waste Plastic into Thin Carbon Nanosheets for Superior Capacitive Energy Storage," *Carbon* 171 (2021): 819–828, https://doi.org/10.1016/j.carbon.2020.09.057.

34. L. Pereira, V. Castillo, M. Calero, G. Blázquez, R. R. Solís, and M. Á. Martín-Lara, "Insights into Using Plastic Waste to Produce Activated Carbons for Wastewater Treatment Applications: a Review," *Journal of Water Process Engineering* 62 (2024): 105386, https://doi.org/10.1016/j.jwpe.2024.105386.

35. H. Ghaedi and M. Zhao, "Review on Template Removal Techniques for Synthesis of Mesoporous Silica Materials," *Energy & Fuels* 36 (2022): 2424–2446, https://doi.org/10.1021/acs.energyfuels.1c04435.

36. M. M. Hasan, R. Haque, M. I. Jahirul, and M. G. Rasul, "Pyrolysis of Plastic Waste for Sustainable Energy Recovery: Technological Advancements and Environmental Impacts," *Energy Conversion and Management* 326 (2025): 119511, https://doi.org/10.1016/j.enconman.2025.119511.

37. H. Yim, S. Valizadeh, G. H. Rhee, et al., "Catalytic Pyrolysis of Harmful Plastic Waste to Alleviate Environmental Impacts," *Environmental Pollution* 343 (2024): 123198, https://doi.org/10.1016/j.envpol.2023.123198.

38. X. Zhu, L. Lin, M. Pang, et al., "Continuous and Low-Carbon Production of Biomass Flash Graphene," *Nature Communications* 15 (2024): 3218, https://doi.org/10.1038/s41467-024-47603-y.

39. J. Ma, C. Yang, X. D. Liu, et al., "Fast Surface Dynamics Enabled Cold Joining of Metallic Glasses," *Science Advances* 5 (2019): aax7256.

40. L. Li, X. Li, Z. Huang, et al., "Joining of Metallic Glasses in Liquid via Ultrasonic Vibrations," *Nature Communications* 14 (2023): 6305, https://doi.org/10.1038/s41467-023-42014-x.

41. A. Hu, Y. Zhao, Q. Hu, et al., "Highly Efficient Solar Steam Evaporation via Elastic Polymer Covalent Organic Frameworks Monolith," *Nature Communications* 15 (2024): 9484, https://doi.org/10.1038/s41467-024-53902-1.

42. S. Xu, J. Zhou, and P. Pan, "Strain-Induced Multiscale Structural Evolutions of Crystallized Polymers: from Fundamental Studies to Recent Progresses," *Progress in Polymer Science* 140 (2023): 101676, https://doi.org/10.1016/j.progpolymsci.2023.101676.

43. C. Song, B. Zhang, L. Hao, et al., "Converting Poly(ethylene terephthalate) Waste into N-Doped Porous Carbon as CO_2 Adsorbent and Solar Steam Generator," *Green Energy & Environment* 7 (2022): 411–422, https://doi.org/10.1016/j.gee.2020.10.002.

44. B. Zhang, C. Song, C. Liu, et al., "Molten Salts Promoting the "Controlled Carbonization" of Waste Polyesters into Hierarchically Porous Carbon for High-Performance Solar Steam Evaporation," *Journal of Materials Chemistry A* 7 (2019): 22912–22923, https://doi.org/10.1039/C9TA07663H.

45. X. Wu, T. Gao, C. Han, J. Xu, G. Owens, and H. Xu, "A Photothermal Reservoir for Highly Efficient Solar Steam Generation without Bulk Water," *Science Bulletin* 64 (2019): 1625–1633, https://doi.org/10.1016/j.scib.2019.08.022.

46. N. Liu, L. Hao, B. Zhang, R. Niu, J. Gong, and T. Tang, "Rational Design of High-Performance Bilayer Solar Evaporator by Using Waste Polyester-Derived Porous Carbon-Coated Wood," *Energy and Environmental Materials* 5 (2022): 617–626, https://doi.org/10.1002/eem2.12199.

47. X. Wen, R. Niu, T. Tang, and J. Gong, "Atmospheric, Continuous Degradation of Poly(ethylene terephthalate) Waste by ZnO," *Applied Catalysis B: Environment and Energy* 377 (2025): 125485.

48. S. Parrilla-Lahoz, E. Jiménez-Páez, M. G. Masteghin, et al., "Upcycling Textile Derived Microplastics Waste Collected from Washer and Dryers to Carbonaceous Products Using Hydrothermal Carbonization," *Waste Management* 200 (2025): 114740, https://doi.org/10.1016/j.wasman.2025.114740.

49. S. Shekoohiyan, A. Sajadi, G. Moussavi, and M. Heidari, "Hydrothermal Carbonization of Plastic Wastes and Effect of Influential Parameters on Performance and Challenges: a Review," *International Journal of Environmental Science and Technology* 22 (2025): 8335–8376, https://doi.org/10.1007/s13762-025-06394-5.

50. K. M. Wyss, K. J. Silva, K. V. Bets, et al., "Synthesis of Clean Hydrogen Gas from Waste Plastic at Zero Net Cost," *Advanced Materials* 35 (2023): 2306763, https://doi.org/10.1002/adma.202306763.

51. D. Liu, S. Zhu, and Q. Mei, "Carbonylolysis of Waste Polyesters into High-Value Organic Acids," *Nature Communications* 17 (2026): 2279, https://doi.org/10.1038/s41467-026-70412-4.

52. X. Huang, W. Ye, J. Zhuang, et al., "π-Conjugated Structure Enhances the UV Absorption Performance of Carbon Dots and Application in the Design of Light-Colored Sunglasses," *ACS Sustainable Chemistry & Engineering* 12 (2024): 10399–10410, https://doi.org/10.1021/acssuschemeng.4c01739.

53. H. Kim, B. Kim, Y. Auh, and E. Kim, "Conjugated Organic Photothermal Films for Spatiotemporal Thermal Engineering," *Advanced Materials* 33 (2021): 28.

54. J. Liu, W. Ruan, H. Zhang, et al., "Highly Efficient Porous Glass Solar Water Evaporator," *Advanced Functional Materials* 35 (2025): 12, https://doi.org/10.1002/adfm.202415394.

55. W. Ruan, H. Zhang, J. Fu, et al., "Dissolution Manufacturing Strategy for Designing Efficient and Low Cost Polymeric Solar Water Evaporator," *Advanced Functional Materials* 34 (2024): 11, https://doi.org/10.1002/adfm.202312314.

56. W. Xu, X. Hu, S. Zhuang, et al., "Flexible and Salt Resistant Janus Absorbers by Electrospinning for Stable and Efficient Solar Desalination," *Advanced Energy Materials* 8 (2018): 1702884, https://doi.org/10.1002/aenm.201702884.

57. H. Bai, N. Liu, L. Hao, et al., "Self-Floating Efficient Solar Steam Generators Constructed Using Super-Hydrophilic N,O Dual-Doped Carbon Foams from Waste Polyester," *Energy & Environmental Materials* 5 (2022): 1204–1213, https://doi.org/10.1002/eem2.12235.

Supporting Information

Additional supporting information can be found online in the Supporting Information section.

Supporting File 1: adma73562-sup-0001-SuppMat.docx.

Supporting File 2: adma73562-sup-0002-VideoS1.mp4.